First-Principles Study of the Structures and Redox Mechanisms of Ni-Rich Lithium Nickel Manganese Cobalt Oxides

I-Ta Hsieh[a], Yuqin Wu[a], Bin Li[b,c], Yue Qi[a*]

[a] School of Engineering, Brown University, Providence, RI, 02912, USA

[b] Energy Science and Technology Directorate, Oak Ridge National Laboratory, Oak Ridge, TN 37830, USA

[c] Oak Ridge Innovation Institute, University of Tennessee Knoxville, Knoxville, TN 37996, USA

Abstract

To reduce the cobalt (Co) content in lithium-ion batteries, Ni-rich (high-Ni) lithium nickel manganese cobalt oxides (NMC) are pursued as one of the next-generation cathode materials. However, there is still debate on the crystal and electronic structures of the baseline, $LiNiO_2$. Density Functional Theory (DFT) calculations were performed to provide a theoretical understanding of Ni-rich NMC. First, it was found that the commonly used $R\bar{3}m$ structure for $LiNiO_2$ is metallic, contrary to the experimentally reported mix-conducting behavior. Among the four different space groups, $R\bar{3}m$, *C2/m*, $P2_1/c$, and *P2/c*, *P2/c* with charge disproportionation of Ni^{2+} and Ni^{4+} is the most energetically stable and semiconducting structure of $LiNiO_2$. Therefore, the atomic structures of representative Ni-rich NMC were built by partially replacing Ni with Co or Mn in the *P2/c* $LiNiO_2$ to form $Li_xNi_yMn_zCo_{1-y-z}O_2$. In the fully lithiated (x=1.0) high Ni content NMC (y>0.5), the oxidation state of all Mn ions becomes 4+, while Co ions still maintain 3+, and part of the Ni ions become 3+ to compensate for the charge. Upon delithiation, the local environment shows more variation of the charge states on the transition metal (TM) ions. The average oxidation on each TM follows a sequence of losing electrons that starts from Ni^{2+} to Ni^{3+}, then oxidizing Ni^{3+} and Co^{3+}, while Mn^{4+} remains electrochemically inactive till x=0. A general relationship for the oxidation state change in each TM as a function of x is derived and shows agreement with both modeling and experimental data.

---

*Corresponding author. Email: YueQi@brown.edu

1. Introduction

The rechargeable Li-ion battery, powered by shuttling lithium ions between cathodes and anodes, has evolved into a pillar of modern society, impacting our daily life from smart phones to electric cars. The overall energy output of the rechargeable Li-ion battery is limited by its cathode due to its relatively lower energy density compared to the anode. Consequently, increasing the voltage and capacity of cathode materials plays a more critical role in increasing the energy density of the Li-ion battery cell. The first commercialized and currently most widely used cathode material is $LiCoO_2$. However, as a result of the cost-prohibitive and controversial sourcing of Co, it is crucial to look for cathode materials with low Co content. Among different cathodes, Ni-rich NMC oxides constructed by a mix of nickel (Ni), manganese (Mn), and cobalt, which have high discharge capacities, working voltage, and high energy densities, are considered among the most promising candidates.[1] However, the source of high capacity, Ni, has proved to be the cause of capacity fade in addition to low thermal stability [2]. Finding a compromise among the Ni/Co/Mn ratio to achieve high energy density, stability (long cycle life and high safety), and cost requires a theoretical understanding of the atomic and electronic structure and redox activity of each transition metal (TM) in the high-Ni NMC cathode. In this endeavor, our research seeks to give a comprehensive understanding of the oxidation state changes in TMs during delithiation. The different oxidation states in TMs correlate with structural stability and degradation mechanisms, such as cation mixing[3], Ni/Li disordering[4], dissolution[5], oxygen release, transformation to spinel, surface reactions, and mechanical stresses associated with Jahn–Teller distortions[6]. The charge state of TMs also varies the electrostatic repulsion between TM and Li ion and thus affects Li diffusion.[7, 8] As a result, nuanced insight into the oxidation state changes in transition metals during delithiation will enable the tailoring of cathode materials to achieve a balanced compromise between high energy density, longevity, and stability, meeting the stringent demands of advanced energy storage applications.

The redox activity in Ni-rich NMC is a complicated phenomenon. First, the transition metal ions in high-Ni NMC cathode are multi-valent, suggesting they could have oxidation states other than 3+ at the fully discharged state. Then the sequence of losing electrons becomes a competition between the electron occupancy on different TM-d and O-2p orbitals. The results ($Li_{1.2}Ni_{0.15}Co_{0.1}Mn_{0.55}O_2$ [9], $LiNi_{1/3}Co_{1/3}Mn_{1/3}O_2$ [10-14], $Li_{1.05}Ni_{0.35}Co_{0.25}Mn_{0.4}O_2$ [15], $LiNi_{0.6}Co_{0.2}Mn_{0.2}\ O_2$ [16, 17], and $LiNi_{0.8}Co_{0.1}Mn_{0.1}O_2$ [18]) generally agree on the oxidation sequence of Ni^{2+}, Ni^{3+} then Co^{3+}, while Mn^{4+} remains electrochemically inactive. Experimentally, the TM oxidation state change can be identified from electron energy loss spectroscopy (EELS)[19-25] and X-ray absorption spectroscopy (XAS)[19, 26-28]. The information is more averaged while the local TM oxidation state may depend on the crystal symmetry, TM mixing, cation exchange[4, 29], Li concentration and oxygen vacancies. In this work, the local electronic properties of a representative NMC811 structure will be calculated and the sequence of losing electrons will be predicted and compared with the experimental observations.

To determine the structure of high-Ni NMC cathode for following computations on the electronic redox activities, it is intuitive to start from the most stable $LiNiO_2$ structure as a parent structure for high-Ni NMC and substitute certain Ni sites with Mn or Co. A space group with rhombohedral symmetry ($R\bar{3}m$) under an α-$NaFeO_2$-type framework, in which oxygen layers pack in an ABCABC sequence, is often constructed as a representative structure of Ni-rich NMC oxides.[30-34] This structure is universally reported by bulk-averaged experimental methods such as X-ray powder diffraction and neutron powder diffraction. However, the $LiNiO_2$ $R\bar{3}m$ structure with Ni being octahedrally coordinated to six oxygen atoms through equivalent Ni–O bonds conflicts with the renowned Jahn–Teller (JT) activity of low-spin trivalent Ni. By means of X-ray absorption techniques and pair distribution functions, the presence of local JT distortions with four short and two long Ni–O bonds in $LiNiO_2$ has been experimentally observed.[35-38] Besides, the $LiNiO_2$-$R\bar{3}m$ structure has been shown to be metallic in density functional theory calculations[39], contrary to the experimentally reported semi-conducting behavior, suggesting the $R\bar{3}m$ structure may not be the correct starting point to study Ni-rich NMC oxides. Since the accurate electronic structure is critical for the understanding of the redox activity in NMC with mixed transition metals, it is required to first determine the correct structure of $LiNiO_2$ and the subsequent structure of Ni-rich NMC.

Because the commonly accepted $R\bar{3}m$ symmetry of $LiNiO_2$ conflicts with the renowned JT activity and the experiment-measured conducting behavior, the symmetry of $LiNiO_2$ structure is still a subject of debate. In the past decade, several theoretical studies have tried to clarify the true ground state structure and give a more detailed insight into the local structure of $LiNiO_2$. Initiated by H. Chen et.al. 's work, [39] three possible monoclinic crystal structures for $LiNiO_2$: *C2/m*, $P2_1/c$, and *P2/c* were introduced. The *C2/m* and $P2_1/c$ structures are Jahn-Teller distorted. While *C2/m* and $P2_1/c$ contain JT elongated Ni-O octahedral, the Ni is mainly 3+ in these structures. The *P2/c* structure does not have distorted transition metal-oxygen octahedrons, but it does allow an oxidation state disproportionation of Ni (Ni^{2+} and Ni^{4+}). It is not the first time that *C2/m* has been examined for α-$NaFeO_2$-type structures. For instance, experiments showed Li_xNiO_2 presented a *C2/m* phase for x in the range from 0.4 to 0.8 [40], and Li_xCoO_2 transformed from the original $R\bar{3}m$ phase into a *C2/m* phase at x around 0.5.[41] Conversely, H. Chen et.al. 's work is the first to propose a crystal structure with *P2/c* space group symmetry as a possible ground-state structure for $LiNiO_2$. In fact, considering the potential energy surface of $LiNiO_2$, all three low-symmetrical structures showed lower energy than the commonly used $R\bar{3}m$ structure. $R\bar{3}m$ is even not a local minimum. Moreover, all three monoclinic structures display semiconducting behavior which agrees with the experiments, while $R\bar{3}m$ is metallic. Recently, several theoretical studies have offered explanations for the puzzling structural properties outlined above. Ab initio molecular dynamics simulations [2, 38, 42] and electron spin resonance studies [43, 44] have suggested the existence of a dynamic and non-cooperativity JT effect in $LiNiO_2$. The continuous and high-frequency reorientation of the JT direction causes the six Ni-O bond lengths measured in the experiment to be equal in length, which are the values of the average of the longer bond and the

shorter bond. These two effects lead to $LiNiO_2$ the commonly accepted macroscopic $R\bar{3}m$ symmetry. In addition, due to the contribution of the electron configurational entropy, the $LiNiO_2$ structure often exists in a high-entropy charge-glasslike state, which is a mix of $P2_1/c$ and $P2/c$ phases, at and below room temperatures.[45] The coexistence of JT distorted and charge disproportion octahedrons in the cell prevent the long-range order in the materials and lead to the observation of an averaged high symmetric structure. Since $R\bar{3}m$ is only a macroscopic average, the low energy structure with correct electronic structures needs to be used as the base $LiNiO_2$ structure to predict the redox activity of Ni-rich NMC.

In this work, First-principles calculations are applied to investigate the crystal structures and electronic structures of Ni-rich NMC oxides. Instead of $R\bar{3}m$, three different space groups, $C2/m$, $P2_1/c$, and $P2/c$ serve as the represented structures of $LiNiO_2$ and the parent structures of its directly related compounds. The search of the ground state structures of $LiNiO_2$ and the base structure for the represented high-Ni NMC oxides is performed by analyzing the electron structures and energy evolutions of the materials. Moreover, the local electronic structure evolutions and the oxidation states changing of transition metals during the delithiation are also investigated. Furthermore, based on the understanding of the oxidation sequences on transition metal ions in representative NMC811, a general oxidation state version lithium content relationship was derived for any high-Ni (y>0.5) in $Li_xNi_yMn_zCo_{1-y-z}O_2$. This general relationship was validated by comparing two compositions, namely NMC811 and NMC622 in experiments.

2. Computational Methods and Justification

In this work, first-principles calculations are performed within the framework of density functional theory (DFT) by the projector augmented wave (PAW) method using the Vienna ab initio simulation package (VASP).[46, 47] DFT calculations are widely applied in high-Ni NMC cathode materials and could help illustrate material properties such as preferential doping sites in host materials[48], the origin of crack generation in [49], oxygen revolutions [50], and phase transformation [41]. Ever since Aydinol et al. [9] used the local-density approximations (LDA) to compute the intercalation voltage of layered $LiMO_2$ cathode materials for various *3d* transition metals (which includes Ni, Co, and Mn) in 1996, the effectiveness of different exchange correlation functionals, including LDA [14], generalized gradient approximations (GGA) [14, 30], GGA+U[30, 32, 51] and GGA+U+D3 [32] were used to reproduce the voltages for NMC333, NMC532 and NMC622 as a function of lithium content and surface properties of NMC811[52], [53]. As noted by Chevrier and Ceder [54], LDA and GGA would underestimate redox potentials for transition metal oxide compounds; adding a Hubbard potential U (GGA+U) could alleviate the problem, but the most accurate predictions are given by the hybrid functional HSE-06 method.[55]

Recognizing the importance and challenges of capturing the correct d-orbital ranking in a multi-TM mixed structure, with GGA+U, the GGA+U calculations performed on single and double transition metal cathode materials will be calibrated with HSE-06. In this work, the Perdue,

Burke, and Ernzerhof (PBE) was used for the exchange–correlation functional [56] and The GGA + U approach is adopted to describe the strongly correlated d electrons of the transition metals.[57] The selection of Hubbard U parameters of 6.5, 4.5, and 4.9 eV for Ni, Mn, and Co ions respectively is determined based on literature[39, 58, 59], where the value of U was proved to be barely relevant to the results of computations. An initial collinear ferromagnetic ordering and magnetic moments of 1.0, 4.0, and 0.0 for Ni, Mn, and Co, respectively, were used. The plane-wave cutoff is set to be 600 eV. The gamma centered Monkhorst–Pack scheme of k-point generation is applied, with k-point spacing less than 0.03 $Å^{-1}$ in the Brillouin zone. Structural optimization is performed for all the cases until the maximum residual force on all atoms becomes less than 0.02 eV-$Å^{-1}$ while the cell is allowed to relax. The geometry optimization and electronic relaxation of single and double transition metal cathode materials are performed within both GGA+U and HSE-06 framework. The oxidation states of transition metal ions are interpreted based on the magnetization results obtained from VASP calibrated with simple known systems. To balance computational accuracy and efficiency, NMC structures with random cation mixing were performed with GGA+U after the calibration with HSE-06.

The model structures representing Ni-rich NMC cathode materials are built by partially replacing Ni with Co or Mn in the base *P2/c* $LiNiO_2$ structure, which is the most energetically stable and semiconducting layered structure of $LiNiO_2$. The oxidation state change of cations Mn and Co are clarified and compared to the redox couples reported in experiments to further examine the efficacy of the computations. This paper also considered the preference of Mn and Co when occupying Ni sites to carefully and systematically simulate the high-Ni NMC cathode materials. It is worth noting that the cells applied in this paper are relatively ordered considering the DFT computation costs. More random structures could be built referring to H. Sun and K. Zhao's work, [33] where they generated 81 configurations for NMC cathodes based on $R\bar{3}m$ structure. Based on the results of this work, random structures built on *P2/c* $LiNiO_2$ with random Co and Mn substitution will serve as a better choice to represent Ni-rich NMC structures.

3. Results and Discussion

3.1 Identifying pure base structures

To identify the pure base structure for Ni-rich NMC oxides, the $LiNiO_2$ is considered within $R\bar{3}m$, *C2/m*, $P2_1/c$, and *P2/c* space groups in unit cells of 12, 8, 8, and 16 atoms respectively. Fig. 1 shows the relaxed crystal structures of $LiNiO_2$ in four different space groups. The lattice parameters, calculated via GGA+U method for these four structures, are listed in Table 1 along with $LiCoO_2$ and $LiMnO_2$ in $R\bar{3}m$ symmetry. As the symmetry changes, the c lattice constant varies, so we listed layer thickness to compare different structures. All four structures share the same "abcabc" oxygen stacking sequence and equal layer thickness of 4.74-4.78 Å. The layer thickness between two adjacent transition metal layers in $LiNiO_2$ is similar to $LiCoO_2$ (4.70 Å) and smaller than $LiMnO_2$ (4.85 Å).

The most notable difference among the three $LiNiO_2$ structures is the shape of the Transition Metal-Oxygen (TM-O) octahedrons and electric properties. In $R\bar{3}m$ $LiNiO_2$, all Ni are Ni^{3+} having equal TM-O bond length of 1.98 Å and β equals 120°, which indicates $R\bar{3}m$ $LiNiO_2$ is hexagonal; In *C2/m* and $P2_1/c$ $LiNiO_2$, all Ni are Ni^{3+} but the octahedrons are elongated along one TM-O bond direction (Fig. 1 (c) and (e)), creating two longer bond lengths and four shorter bond lengths. The result agrees with the experimental measurements, with the shorter bonds 1.91 Å and the longer bonds 2.09 Å, leading to an overall average bond length of 1.97 Å[35]; In *P2/c* $LiNiO_2$, Ni is allowed in two oxidation states: Ni^{2+} and Ni^{4+}. The Ni^{2+}-O bonds range from 2.04 Å to 2.06 Å, while the Ni^{4+}-O bonds are between 1.87 Å and 1.88 Å. In Fig 1. (f) and (g), the two types of TM-O octahedrons are differentiated by color: orange represents the slightly larger Ni^{2+}-O octahedrons and yellow represents the smaller Ni^{4+}-O octahedrons. All the *C2/m*, $P2_1/c$, and *P2/c* $LiNiO_2$ are monoclinic structures with non-equal TM-O bond lengths in them. Moreover, semiconductor band gaps emerge in all three monoclinic structures while the $R\bar{3}m$ $LiNiO_2$ has a metallic behavior.

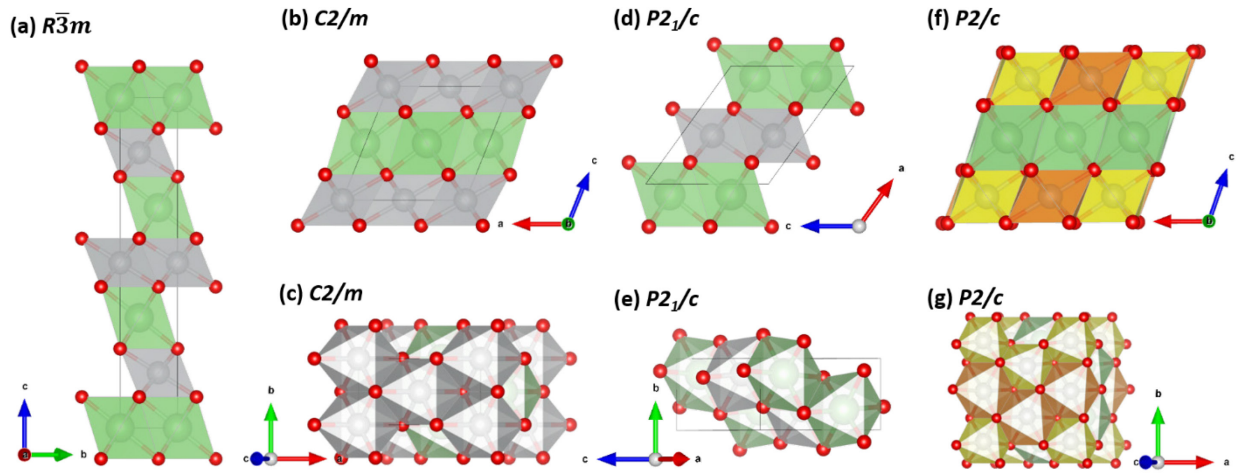

Fig 1. Representative crystal structures of $LiNiO_2$. Red spheres represent oxygen, green spheres represent lithium, orange spheres represent Ni^{2+}, silver spheres represent Ni^{3+} and yellow spheres represent Ni^{4+}. (a) side view of the $R\bar{3}m$ cell. (b) side view of the *C2/m* cell. (c) top view of the *C2/m* cell. (d) side view of the $P2_1/c$ cell. (e) top view of the $P2_1/c$ cell. (g) side view of the *P2/c* cell. (g) top view of the *P2/c* cell

Table 1. The unit cell parameters, transition metal (TM)-O bond lengths, band gap, layer thickness (lithium layer and transition metal layer), TM magnetic moment and normalized stabilization energies (relative to the R$\bar{3}$m cell).

	$LiCoO_2$-$R\bar{3}m$	**$LiMnO_2$-$R\bar{3}m$**	**$LiNiO_2$-$R\bar{3}m$**	**$LiNiO_2$-*C2/m***	**$LiNiO_2$-$P2_1/c$**	**$LiNiO_2$-*P2/c***
a(Å)	2.82	3.10	2.88	5.13	5.83	4.92
b(Å)	2.82	2.86	2.88	2.77	2.92	5.78
c(Å)	14.17	14.72	14.34	5.12	4.88	5.01
γ/β(°)	120	118	120	112	125	109
Layer thickness(Å)	4.70	4.85	4.78	4.75	4.74	4.74

Band gap(eV)		2.70	1.13	Metallic	0.32	0.37	0.75
d_{TM-O}(Å)		1.93	1.96, 2.33	1.98	1.89, 2.13	1.90, 2.10	2.04 - 2.06 (Ni^{2+}) 1.87 - 1.88 (Ni^{4+})
TM Mag. Mom. (μB) and charge (Q) [a]		0 (Co^{3+})	3.91 (Mn^{3+})	1.41 (Ni^{3+})	1.08 (Ni^{3+})	1.12 (Ni^{3+})	1.77 (Ni^{2+}) 0.09 (Ni^{4+})
Energy [b] f.u. (meV)	GGA+U			0	-64.61	-70.29	-78.06
	vdW			0	-59	-64	-73

[a] TM ion Magnetic Moment (μB) and the classical charge state (Q)

[b] Energy / f.u. with respect to that of $R\bar{3}m$ symmetry

The oxidation states on Ni are defined by the magnetic moment (μB listed in **Table 1 and Table S1**) and their electronic structures (**Fig. S2)**. The integer oxidation state is a convenient description for transition metal oxides, although mixed ionic and covalent bonds with partial electron transfers are more accurate. Our previous studies have shown the magnetic moment is more reliable and sensitive to the integer oxidation states on transition metals than the Bader charge analysis. [60] In this study, we first calibrated the magnetic moment with known charge states in simpler systems (e.g. $LiCoO_2$, $LiMnO_2$, and $LiNiO_2$) and used them to indicate the charges in a mixed cation system. For example, with no unpaired electrons, Co^{3+} and Ni^{4+} showed μB close to zero, in $LiCoO_2$-$R\bar{3}m$ and one site in $LiNiO_2$-P2/c. The μB for Ni in $LiNiO_2$-$R\bar{3}m$ is close to the ideal value of Ni^{3+} with one unpaired electron. It is increased and decreased in $LiNiO_2$-P2/c, corresponding to the charge disproportionate change. Since the computed μB aligns well with the low spin electronic configurations in the three transition metals, we did not separately project d-orbitals into t_{2g} and e_g in the PDOS plot. Fig. 2 plots the total density of states (DOS) and the projected DOS (PDOS) for Ni and O atoms of the three structures, where the PDOS plots only include the Ni-3d or O-2p orbitals of an individual ion, since all the ions of the same kind share the same electronic characteristics. The comparison of the three total DOS plots on the right panel of **Fig. 2** showed that the $R\bar{3}m$ structure is metallic, while the *C2/m*, *P2₁/c*, and *P2/c* structures have a band gap of 0.32 eV, 0.37 eV and 0.75 eV, respectively. Metallic $LiNiO_2$ is contradictory to previous experimental studies that proved $LiNiO_2$ is a small-gap semiconductor of around 0.5 eV [61]. Notably, the fermi level in all the DOS plots is referred to as 0, below which the states are occupied. The colored PDOS plots on the left of Fig. 2 along with the individual cation PDOS (Fig S2 in SI) separate the contribution of different ions so that the disparate electronic characteristics of the three nickel ions can be clearly observed: in $R\bar{3}m$, the correlated Ni-3d and O-2p orbitals contain the fermi level, indicating a metallic behavior; in *P2/c*, the up and down two unoccupied states belong to Ni^{4+}, corresponding to its electron configuration of $t_{2g}^6e_g^0$; while no obvious unoccupied state could be found around fermi level belonging to the high-spin Ni^{2+} ($t_{2g}^6e_g^2$). In *C2/m* and *P2₁/c*, the unoccupied state above fermi level conforms to the electron configuration $t_{2g}^6e_g^1$ of Ni^{3+}. We interpreted Ni charges as "3+" if they show uniform charge in LiNiO2. However, The Ni^{3+} in C2/m and $P2_1/c$ structures showed fewer unpaired electrons than that in $R\bar{3}m$, consistent with the lower μB values. In fact, in the low-spin metal complex with such

an asymmetric electron occupancy (Ni^{3+}: $t_{2g}^6e_g^1$), a strong Jahn-Teller distortion is expected to occur to stabilize electrons and orbital ordering.

It was known that GGA typically underestimates the band gap, and GGA+U can predict a more accurate band gap. To validate the U-parameters used in the GGA+U method, the more accurate hybrid functional HSE-06 was also performed. The total density of states of the HSE-06 calculation also shows $LiNiO_2$ in a $R\bar{3}m$ cell should be metallic (**Fig. S1**). Both methods predict that $LiNiO_2$ with an $R\bar{3}m$ symmetry is metallic.

Table 1 also lists the energies of these structures. The energy of *C2/m, $P2_1/c$*, and *P2/c* $LiNiO_2$ are lower than the $R\bar{3}m$ structure by 65 meV, 70 meV, and 78 meV, respectively, similar to that reported by H.Chen[39], while the energies of three monoclinic structures are lower than $R\bar{3}m$ structure by 59 meV, 64 meV, and 73 meV by considering vdW-correction in the calculations. Although the energy difference among the four $LiNiO_2$ structures is only less than 0.1 eV, their band structures show drastic differences. Since the $LiNiO_2$ with an $R\bar{3}m$ symmetry is metallic, against experimental observations, it can be determined that *C2/m $P2_1/c$*, and *P2/c* structures are more reasonable base structures for Ni-rich NMC cathode materials in computations and will be applied in the later discussions.

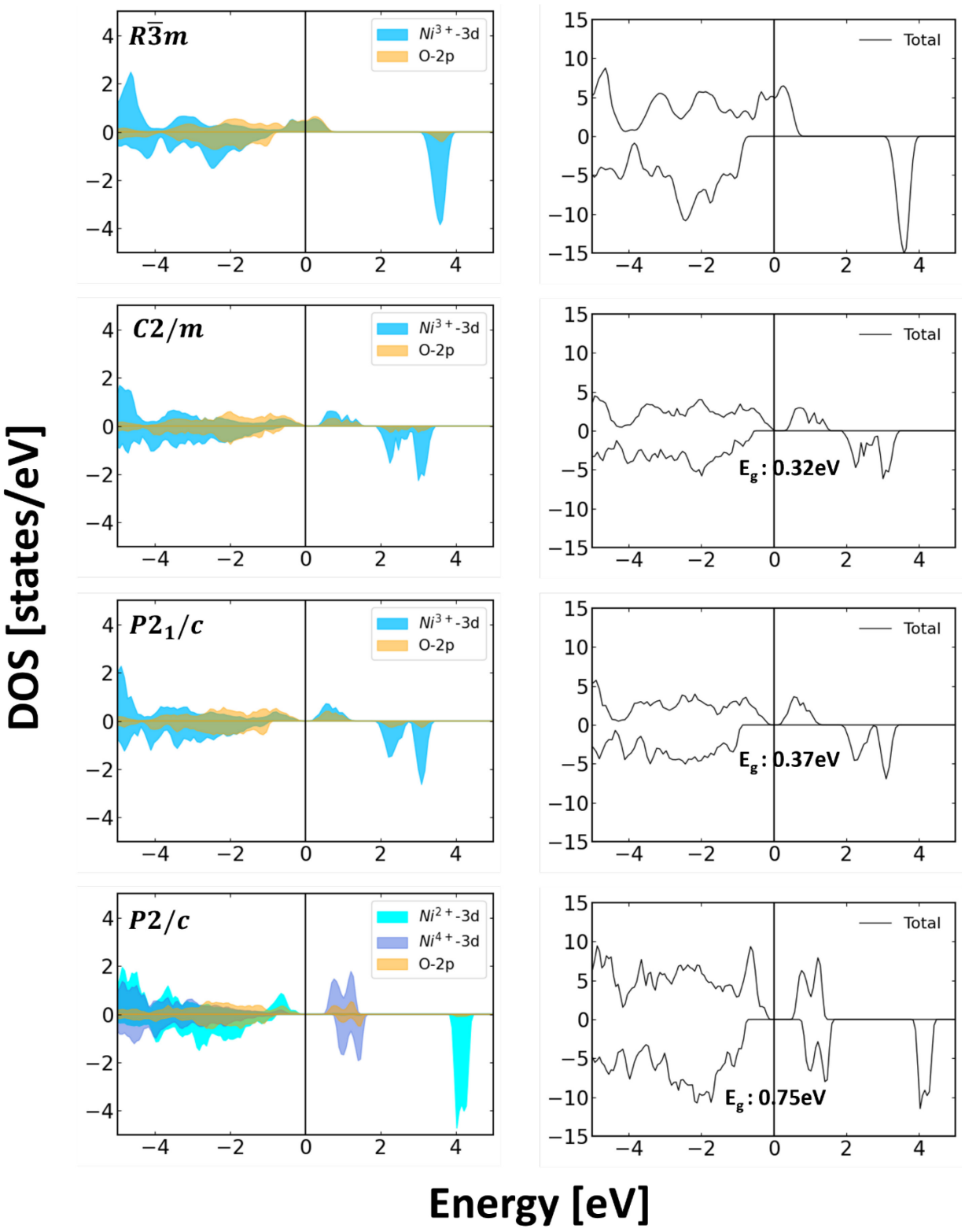

Fig 2. Projected density of states (PDOS) and total density of states of the four different unit cells for $LiNiO_2$. Yellow represents O-2p orbitals, and the shades of blue represent Ni-3d in all four different unit cells, with blue representing Ni3+-3d while light-blue and dark-blue representing Ni2+-3d and Ni4+-3d in P2/c unit cell, respectively.

3.2 Substituting Ni with Co/Mn

Due to the lower symmetry of *C2/m, P2₁/c,* and *P2/c* $LiNiO_2$ structures, there are multiple options for Co and Mn to substitute a Ni site. Since Ni exhibits 2+ and 4+ in the *P2/c* structure and 3+ in the *C2/m and P2₁/c* structure, it is unclear if Co or Mn has any preference for substituting Ni at a specific oxidation state. This is an additional challenge compared to generating random structures based on $R\bar{3}m$ structure [33]. Therefore, the oxidation states of Ni, Mn, and Co in a $Li_xNi_yMn_zCo_{1-y-z}O_2$. structure needs to be investigated. In a typical NMC811 metal oxide, where non-Ni transition metal ions only occupy 10% of the total number of transition metal ions, it is acceptable to assume a dilute approximation that Mn and Co are independent when occupying Ni sites.

Therefore, the aforementioned questions could be first simplified and discussed in binary systems, namely $Li(NiMn)O_2$ and $Li(NiCo)O_2$, where the substitution behavior of Mn and Co are studied separately. To identify the preference of Mn and Co when doping in the different sites in $LiNiO_2$, $LiNi_{0.5}Mn_{0.5}O_2$ and $LiNi_{0.5}Co_{0.5}O_2$ are built with *C2/m*, *P2₁/c*, and *P2/c* symmetry in 2 × 3 × 1 (48 atoms), 2 × 2 × 2 (64 atoms), and 2 × 2 × 1 (64 atoms) supercells, respectively. These ordered structures with different configurations are used to give insight into the competition of the charge states with mixed cations. The DFT computed binary mixing free energy with respect to the pure $LiMO_2$ is defined as

$$G_{mix} = E(mixed) - \alpha_{M_1} E_{Li(M_1)O_2} - \alpha_{M_2} E_{Li(M_2)O_2} + N k_B T(\alpha_{M_1} \ln \alpha_{M_1} + \alpha_{M_2} \ln \alpha_{M_2}), \qquad \text{(Eq. 1)}$$

where E is the energy calculated by DFT and α is the fraction of transition metal M_1 and M_2 in the compound.

Table 2 records the magnetic moments, μB, and the oxidation states of all the transition metal (TM) ions in the $LiNi_{0.5}Mn_{0.5}O_2$ and $LiNi_{0.5}Co_{0.5}O_2$ cells calculated by using both GGA+U and HSE-06 methods, which are compared in order to test if GGA+U along with the U-parameters used can capture the correct oxidation states in oxides with mixed transition metal cations. The eight columns in **Table 2** represent Mn and Co occupying the four inequivalent doping sites, the Ni^{3+} site in *C2/m* and *P2₁/c* as well as the Ni^{2+} and Ni^{4+} sites in *P2/c*, in both $LiNi_{0.5}Mn_{0.5}O_2$ and $LiNi_{0.5}Co_{0.5}O_2$. By observing the charge states of Mn (the left half of Q™ in **Table 2**), it is easy to notice that for $LiNi_{0.5}Mn_{0.5}O_2$, no matter which site Mn occupies, Mn is always oxidized to the Mn^{4+} state, and correspondingly, the remaining Ni becomes Ni^{2+}. Both GGA+U and HSE-06 methods give the same oxidation states for Mn and Ni, meaning the substitution site of Mn does not have preference. In other words, Mn can subsite either the Ni^{2+} or the Ni^{4+} sites within the *P2/c* structure, and the final states are the same after relaxation. This is further correlated with the same formation energy (-436 meV for GGA+U and-342 meV for HSE-06) of the two relaxed *P2/c* $LiNi_{0.5}Mn_{0.5}O_2$ with different Ni occupancies. *P2/c* type $LiNi_{0.5}Co_{0.5}O_2$, however, exhibited different behavior. After Co substitution, HSE results suggest that Co and Ni both exhibit 3+ charges. GGA+U results agree with the HSE results with one exception, that is when Co occupying Ni^{4+} sites in *P2/c* structures, the GGA+U computation reports Ni^{2+} and Co^{4+}. Moreover,

considering the mixing free energy, it is also thermodynamically unstable when Co occupying Ni^{4+} sites in *P2/c*. This result is likely due to the insufficient accuracy of GGA+U when describing systems with both localized and delocalized electronic states.[50]

Table 2. Oxidation state, Q, interpreted from magnetic moment, μB, of transition metal ions when mixing Mn or Co into pure $LiNiO_2$ to form ordered $LiNi_{0.5}Mn_{0.5}O_2$ and $LiNi_{0.5}Co_{0.5}O_2$.

Composition			$LiNi_{0.5}Mn_{0.5}O_2$				$LiNi_{0.5}Co_{0.5}O_2$			
Original Symmetry			***C2/m***	***P2₁/c***	***P2/c***		***C2/m***	***P2₁/c***	***P2/c***	
Ni Substituted			**(Ni^{3+})**	**(Ni^{3+})**	**(Ni^{2+})**	**(Ni^{4+})**	**(Ni^{3+})**	**(Ni^{3+})**	**(Ni^{2+})**	**(Ni^{4+})**
Ni	**μB**	GGA+U	1.79	1.79	1.79	1.79	1.31	1.12	1.17	1.59
		HSE	1.69	1.69	1.70	1.70	0.90	0.86	0.84	0.86
	Q	GGA+U	2+	2+	2+	2+	3+	3+	3+	2+
		HSE	2+	2+	2+	2+	3+	3+	3+	3+
TM	**μB**	GGA+U	3.25	3.08	3.26	3.26	0.03	0.02	0.04	1.85
		HSE	3.08	2.93	3.08	3.08	0.03	0.01	0.00	0.00
	Q	GGA+U	4+	4+	4+	4+	3+	3+	3+	4+
		HSE	4+	4+	4+	4+	3+	3+	3+	3+
G_{mix} (meV)		GGA+U	-348	-314	-436	-436	7	-49	-41	50
		HSE	-161	-429	-342	-342	215	-52	-57	214

Table 3. Oxidation state, Q, and magnetic moment, μ, of transition metal ions in $Li_xNi_{0.5}Mn_{0.5}O_2$ and $Li_xNi_{0.5}Co_{0.5}O_2$ (x=1, 0.5, 0).

	$Li_xNi_{0.5}Mn_{0.5}O_2$ (*P2/c*)				**$Li_xNi_{0.5}Co_{0.5}O_2$ (*P2/c*)**			
	Ni		**Mn**		**Ni**		**Co**	
	μB	**Q**	**μB**	**Q**	**μ**	**Q**	**μ**	**Q**
x = 1	1.8	2+	3.3	4+	1.2	3+	0	3+
x = 0.5	1.1	3+	3.3	4+	0	4+	0	3+
x = 0	0.3	4+	3.3	4+	0.1	4+	1.3	4+

Starting from the $Li_xNi_{0.5}Mn_{0.5}O_2$ and $Li_xNi_{0.5}Co_{0.5}O_2$ *P2/c* cells, half-delithiated and fully-delithiated structures were calculated by randomly removing Li atoms. **Table 3** shows the magnetic moment and charge states on the TM cations. During delithiation, the Ni in $LixNi_{0.5}Mn_{0.5}O_2$ (x=1, 0.5, 0) changes from 2+ to 3+ and to 4+ while Mn^{4+} remains the same charge; suggesting Ni^{2+} and Ni^{3+} are redox active and Mn^{4+} is not. In contrast, both Ni and Co are 3+ in $LiNi_{0.5}Co_{0.5}O_2$. During delithiation, Ni^{3+} is oxidized to Ni^{4+}, suggesting it is redox active first. This is reasonable by considering the electron occupancy of Ni^{3+} ($t_{2g}^6e_g^1$) and Co^{3+} ($t_{2g}^6e_g^0$), it is easier for Ni to lose its unpaired e_g^1 electron. After Ni^{3+} is oxidized to Ni^{4+}, both Ni^{4+} and Co^{3+} have fully filled t_{2g} orbitals, so the less oxidized Co^{3+} becomes easier to oxidize than Ni^{4+} as shown in **Table 3** within the range of x=0.5 to 0.

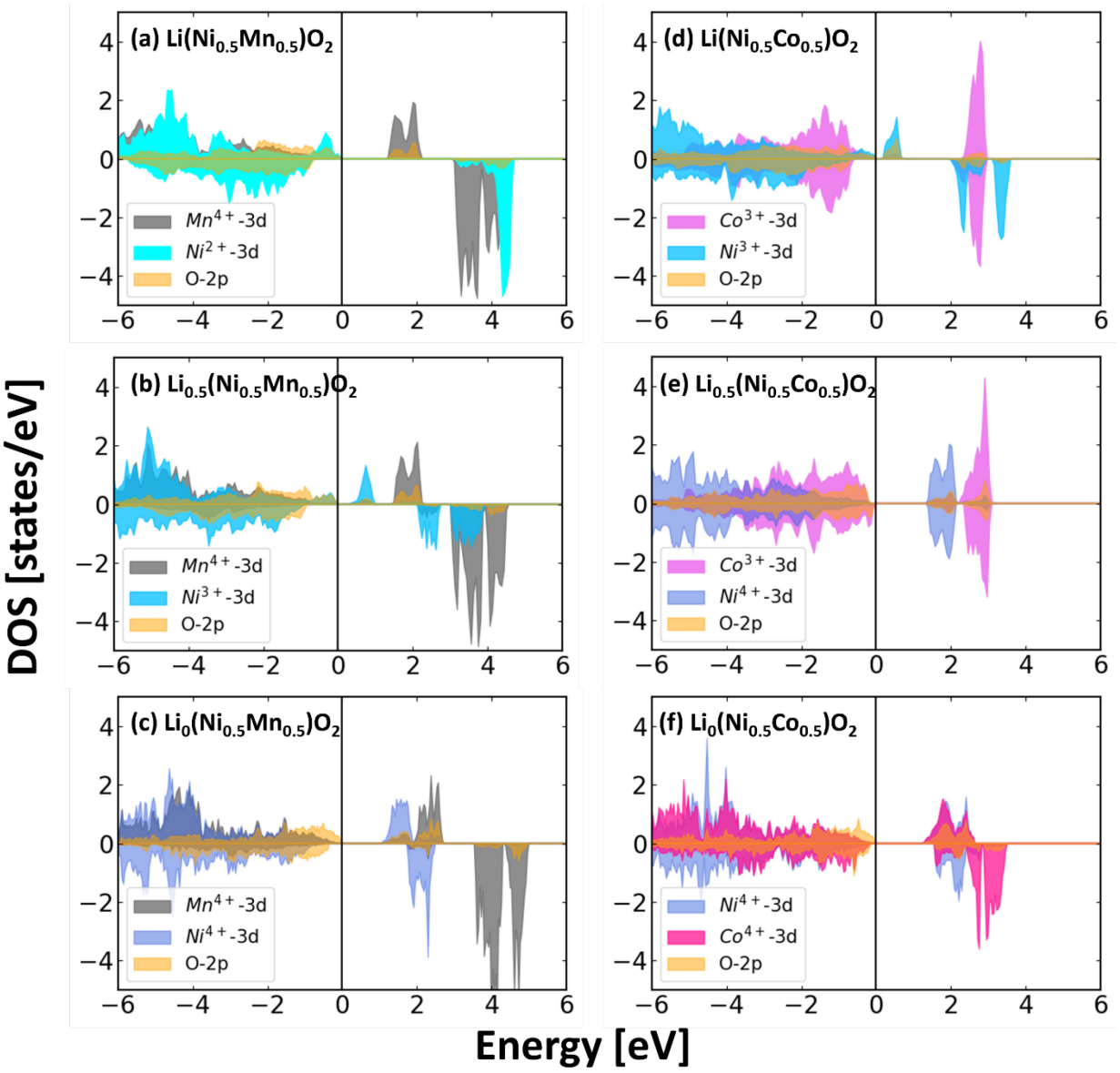

Fig 3. PDOS of the P2/c unit cells for $Li_xNi0.5Mn_{0.5}O_2$ and $Li_xNi0.5Co_{0.5}O_2$ (x=1, 0.5, 0). Yellow represents O-2p orbitals, shades of blue represent Ni-3d, gray represents Mn^{4+}-3d, and shades of red represent Co-3d, respectively. (a) $LiNi_{0.5}Mn_{0.5}O_2$. (b) $Li_{0.5}Ni_{0.5}Mn_{0.5}O_2$. (c) $Li_0Ni_{0.5}Mn_{0.5}O_2$. (d) $LiNi_{0.5}Co_{0.5}O_2$. (d) $Li_{0.5}Ni0.5Co_{0.5}O_2$. (f) $Li_0Ni_{0.5}Co_{0.5}O_2$. Note that when de-lithiation, the sequence of losing electrons is: Ni^{2+}, Ni^{3+}, Co^{3+} and Mn^{4+}.

The PDOS shown in **Fig. 3** further verifies the above changes for $LixNi_{0.5}Mn_{0.5}O_2$ and $LixNi_{0.5}Co_{0.5}O_2$ (x=1, 0.5, 0) *P2/c* unit cells during delithiation. In line with the conclusions from **Table 3**, that Mn stays as the highly oxidized Mn^{4+} during delithiation, the DOS plots of Mn (gray) remain almost unchanged in (a), (b) and (c) at different stages of delithiation. In contrast with Ni,

of which the DOS plots (shades of blue) keep changing shape, and when the structure is fully delithiated, DOS becomes highly symmetrical, implying the zero spin of Ni^{4+} ($t_{2g}^6e_g^0$). It is noted that due to p-d hybridization between O-2p orbitals and TM-3d orbitals, the features of the PDOS for O-2p and TM-3d are essentially identical around fermi level (the overlapping states of TM and O). **Fig 3(a) and 3(b)** prove that as a result of the notable high oxidization of Mn^{4+}, electrons can only be lost from Ni^{2+} and Ni^{3+}, where the states under the fermi level belong to Ni-3d orbitals and hybridized O-2p orbitals. Similar analyses could be applied to $Li_xNi_{0.5}Co_{0.5}O_2$ (x=1, 0.5, 0) in **Fig. 3 (d), (e) and (f)** that electrons start to lose from Ni^{3+} and then Co^{3+}. The unoccupied states around fermi level in **Fig. 3(d)** disappear in **Fig. 3(e)** after the removal of half of the Li ions, conforming to the oxidation change from Ni^{3+} ($t_{2g}^6e_g^1$) to Ni^{4+} ($t_{2g}^6e_g^0$). In **Fig. 5(e)**, both Ni^{4+} ($t_{2g}^6e_g^0$) and Co^{3+} ($t_{2g}^6e_g^0$) have a symmetrical electron occupancy in $Li_{0.5}Ni_{0.5}Co_{0.5}O_2$. The GGA+U computation demonstrated that electrons will be lost from the higher red peaks belonging to Co^{3+} in **Fig. 3(e)** and shift the t_{2g} orbitals upward in energy (**Fig. 3(f)**).

It is no accident that Mn and Co have different behaviors in the delithiating process. According to the energy levels of potentially active orbitals, Ni^{3+} and Mn^{3+} redox involve less stable electron configurations in e_g orbitals, combined with the fact that redox couple Ni^{2+}/Ni^{3+} and Ni^{3+}/Ni^{4+} are lower in energy than Mn^{3+}/Mn^{4+}, and all the three redox couples include the relatively unstable e_g orbital. That indicates Mn^{3+} is possible to donate electrons to Ni ions spontaneously, and thus yields Mn^{4+} and reducing Ni ions. [6, 62, 63] As a result, Mn keeps in an oxidation state of 4+ during the entire process if the concentration of Mn is not higher than Ni in the compound (Fig. S4). In contrast, Co does not have similar behavior because the redox couple Co^{3+}/Co^{4+} with a low-spin Co^{3+} happens in the relatively stable t_{2g} orbital.

3.3 Building NMC811 model system

Higher-Nickel content in NMC cathode is desired, thus NMC811 is one of the most high-profile candidates. Based on the energy in **Table 1** as well as G_{mix} and the predicted oxidation states in **Table2**, in this work, *P2/c* $LiNiO_2$ will serve as a base structure to build the Ni-rich NMC cathodes. Since GGA+U has given reasonable agreement with HSE-06 results, it will be used for the following studies. To avoid possible discrepancies, Co will be allowed to substitute only Ni^{2+} sites in the following GGA+U calculations.

To determine a representative NMC811 atomic structure, several attempts have been made in this paper. First, a smaller trail $Li(Ni_{0.875}Mn_{0.0625}Co_{0.0625})O_2$ cell is built in a 2×2×1 *P2/c* supercell with 64 atoms, of which Ni : Mn : Co = 14 : 1 : 1. The expansion along a and b vectors creates more possibilities of Mn and Co occupying the existing Ni sites. Here we consider three configurations regarding the atomic distance between Co and Mn in the crystal. Each TM-O octahedron is surrounded by six nearest neighbor octahedrons, the six nearest neighbor octahedrons constitute the so-called first neighbor ring (1NR). Subsequently, the terms second neighbor ring (2NR) and third neighbor ring (3NR) refer to the second and third layers of nearest-

neighbor octahedrons, respectively. Taking the Mn-O octahedron as the center, three configurations were created by extending the location of Co from the first ring to the third ring. The structures of three distributions and predicted oxidation states of cations are demonstrated in Fig. S6. The energy of the three configurations only differs by 0.01 eV/f.u, which is negligible. Therefore, the energy is not strongly dependent on Co-Mn distance, i.e. Co-Mn correlation can be neglected in a high-Ni NMC oxide.

To further increase the randomness while sustaining the efficiency of DFT computations, a $Li(Ni_{0.75}Mn_{0.125}Co_{0.125})O_2$ structure (Ni : Mn : Co=24 : 4 : 4) with 128 atoms is built by expanding *P2/c* unit cell to a 2×2×2 supercell (Fig. S5a). The configurations of layer 1 and layer 2 along the layer stacking direction are designed differently to increase randomness. The energy comparison of the three configurations in Fig. S6 shows that the effect of Co and Mn distribution is negligible (energy difference smaller than 0.01eV/f.u.). Therefore, the configurations of layer 1 and layer 2 are arbitrarily assigned.

In comparison to this manually-built random 2×2×2 structure, the widely used special quasi-random structures (SQS) method is also applied to find another random $Li(Ni_{0.75}Mn_{0.125}Co_{0.125})O_2$ with the same stoichiometry and number of atoms but different configurations. Here we apply the Monte Carlo Special Quasi random Structure (MCSQS)[64] algorithm designed by Van de Walle et al. as part of the alloy theoretic automated toolkit (ATAT) to identify another random structure. When calculating the target correlations, the empty clusters are ignored and the cutoffs for the pairs and triplets are specified as 2.9Å and 5Å, respectively. The cutoffs are determined by the nearest and second nearest site distances. For the ternary random structure, the maximum correlation mismatch is smaller than 0.05. The MCSQS produced 222 structure is displayed in Fig. S5b, which has an energy of 0.08 eV/f.u. higher than the manually built 222 structure shown in Fig S5a. This minor difference further supports our conclusion that the energetic dependence on Co and Mn distribution is not strong in high Ni-NMC. Among the 221, 222, and SQS structures, the manually-built *P2/c*-based $Li(Ni_{0.75}Mn_{0.125}\ Co_{0.125})O_2$, i.e. 222, is the most stable one and is hereby chosen as the representative NMC811 structure.

3.4 Redox properties of the NMC811 model system

The Open-circuit voltage (OCV) of the representative NMC811 is computed with DFT and compared with experiments. The OCV is the chemical potential difference between the cathode and anode. In a case of redox reaction $Li_{x1}MO_2 + (x_2\text{-}x_1)\ Li \rightarrow Li_{x2}MO_2$, where TM could be the transition metal ions Ni, Mn, and Co or the binary and ternary combinations of them. The OCV is therefore calculated as [56, 57, 65]

$$OCV = -\frac{E[Li_{x_2}MO_2]-E[Li_{x_1}MO_2]-(x_2-x_1)E[Li]}{(x_2-x_1)e} \quad (2)$$

where E is the DFT-calculated total energy and e is the electron charge. Here, the voltages are considered in two composition ranges $[x_2, x_1] = [1, 0.5]$ and $[x_2, x_1] = [0.5, 0]$. The half-delithiated

structures were built by the removal of the appropriate number of Li atoms from the fully-lithiated counterparts.

Table 4. Open-circuit voltage (OCV) of the batteries with different cathodes.

	Without vdW-correction			**With vdW-correction**		
	[x_2, x_1] = [1, 0.5]	**[x_2, x_1] = [0.5, 0]**	**Average**	**[x_2, x_1] = [1, 0.5]**	**[x_2, x_1] = [0.5, 0]**	**Average**
$LiNiO_2$	3.87	3.99	3.93	3.84	3.96	3.90
$LiNi_{0.5}Mn_{0.5}O_2$	3.96	4.23	4.10	3.93	4.17	4.05
$LiNi_{0.5}Co_{0.5}O_2$	3.54	4.15	3.85	3.62	4.14	3.88
$Li(Ni_{0.75}Mn_{0.125}Co_{0.125})O_2$	3.88	4.03	3.96	3.86	3.98	3.92

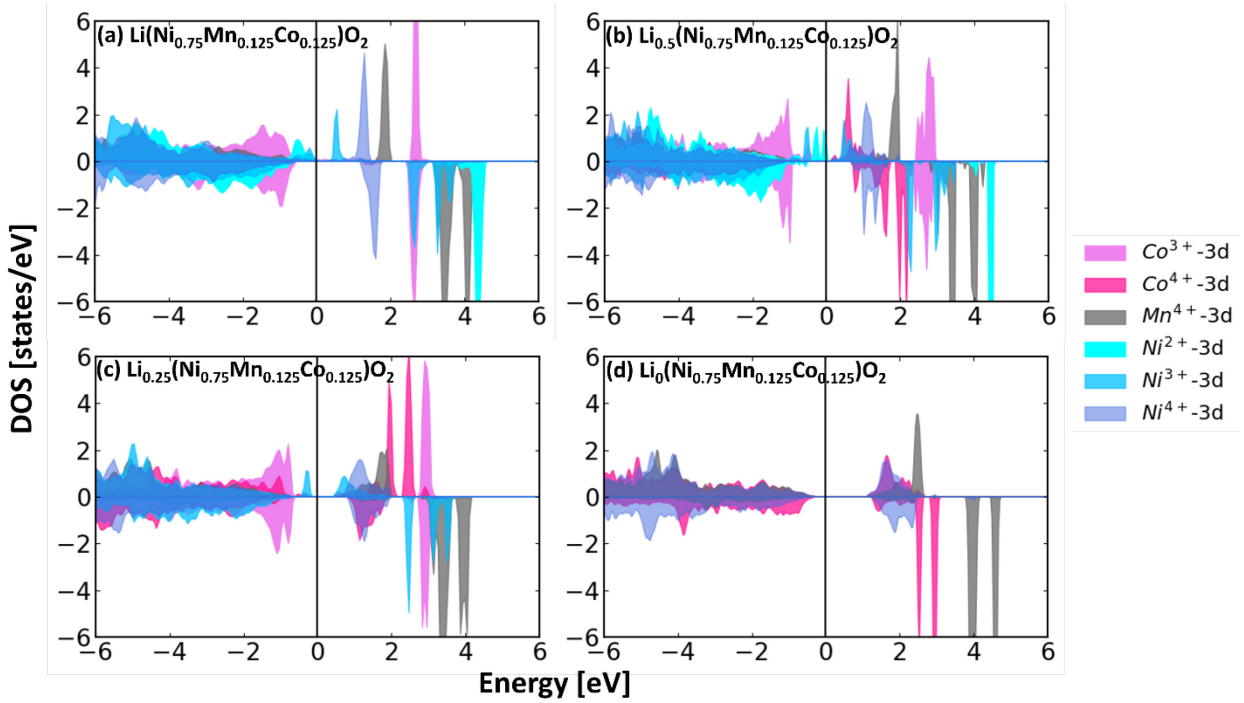

Fig 4. PDOS of NMC811 ($Li_xNi_{0.75}Mn_{0.125}Co_{0.125}O_2$). Shades of blue indicate Ni, gray indicates Mn, and shades of red indicate Co. The meanings of symbols and colors are the same as in Fig 2 and 3. PDOS of (a) x=1 (fully-lithiated), (b) x=0.5 (c) x=0.25, and (d) x=0 (fully-delithiated) NMC811.

Table 4 listed the OCV of this NMC811 structure along with the pure phase $LiNiO_2$ and the binary $LiNi_{0.5}Mn_{0.5}O_2$ and $LiNi_{0.5}Co_{0.5}O_2$. Both with and without vdW-corrections were considered in the DFT computation. The average computed intercalation voltage of $LiNiO_2$, which is 3.93 V (without vdW-correction) or 3.90V (with vdW-correction), is in good agreement with experiment [66] (Fig. S7a), but is higher than the 3.3 V predicted by Y. Koyama et. al.[14], who

employed LDA and GGA approaches. On the other hand, our computed average intercalation voltage of $Li(Ni_{0.75}Mn_{0.125}Co_{0.125})O_2$, which is 3.96 V (without vdW-correction) or 3.92V (with vdW-correction), is in good agreement with experiment [67, 68] (Fig. S7b).

Another comparison to the experiment can be made is the characteristic anisotropic response in the in-plane and out-plane lattice parameters as a function of lithium concentration in $LiNiO_2$ and NMC811 [18, 40, 69-71]. During delithiation, lattice parameters a and b decrease (Fig. S9a) while the c-axis first expanse in the early stage of delithiation and rapid shrink, characterized as the H2–H3 phase transformation with further Li-extraction (Fig. S9b), which agrees well with experiments [40, 72]. The evolution of the volume and lattice parameters can be well described when vdW-corrections are considered as shown in Fig S9. However, the calculated electronic properties with and without vdW-corrections are similar (Fig. S10 and S11).

To capture the changes in the electronic properties and oxidation states and verify the redox sequence, a delithiating process of the fully-lithiated oxide $Li(Ni_{0.75}Mn_{0.125}Co_{0.125})O_2$ is considered, where the initial oxidation states are 2+/3+/4+, 4+, and 3+ for Ni, Mn, and Co, respectively, as shown in **Fig. 4(a)**. During delithiation, the electronic characteristics and oxidation states of transition metal ions are going to change correspondingly. As indicated by the PDOS plots in **Fig. 4**, the oxidation starts from Ni^{2+} becoming Ni^{3+}, and followed by Ni^{3+} to Ni^{4+}. Co^{3+} starts to oxidize to Co^{4+} after some Ni^{2+} and Ni^{3+} already become Ni^{3+} and Ni^{4+}. If further charging the battery, all the Ni and Co eventually become 4+. Mn stays in oxidation state 4+ since the concentration of Mn is lower than Ni in the compound. The magnetic moments for transition metals during delithiation is shown in Fig. S8. Again, the PDOS only plots a single ion of each kind, since all the ions of the same kind share similar electronic characteristics, as stated in **section 3.1.**

To obtain a more general understanding of the oxidation sequence of each TM ion in the Ni-rich NMC materials, we derived the equations that could capture evolutions of the average valence of Ni and Co during the delithiation by observing the trend of the changing in oxidation state of Ni and Co in the experiment and DFT calculations. In general, the high-Ni NMC compound could be written in a formula $Li_xNi_yMn_zCo_{1-y-z}O_2$. Consider the case that $y > 0.5$ and $y > 2z$, the Mn will be 4+ and the ratio of each Ni and Co ion with different oxidation states is noted as N_{Ni}^{n+} and N_{Co}^{n+}, respectively. Their relationship with x,y, and z are listed in **Table 5**. For example, when x=1, all Co are 3+ and N_{Co}^{3+}=1-y-z, the number ratio of Ni2+, 3+, 4+ is $\frac{y}{2}$, z, and $\frac{y}{2} - z$, respectively. In the first stage of delithiation, Ni^{2+} oxidized to Ni^{3+} first, so N_{Ni}^{2+} decreases and N_{Ni}^{3+} increases with (1-x), where (1-x) is the amount of removed Li; while other species remain the same. Ni^{3+} and Co^{3+} start loss electrons after all Ni^{2+} became Ni^3, which starts at $x_c = 1 - \frac{y}{2}$. The average oxidation states of Ni and Co can be computed according to N_{Ni}^{n+} and N_{Co}^{n+}.

The equations in **Table 5** also predicted the evolution of average oxidation states, which can be further applied to experimental NMC ratios and experimental measurements. Fig 5 (a) showed the predicted average oxidation states compared well with DFT predictions

$LiNi_{0.75}Mn_{0.125}Co_{0.125}O_2$ and experiment measurements $LiNi_{0.8}Mn_{0.1}Co_{0.1}O_2$ [72]. Fig 5 (b) shows the predicted NMC622 oxidation state change compared well with the experiment measurements[17]. Moreover, a trial of using these equations to predict **NMC811, also agreed well with a new DFT calculation and experiment measurements**[72] **on a random $LiNi_{0.8}Mn_{0.1}Co_{0.1}O_2$ structure built** by MCSQS code (Fig 5c). Despite the local oxidation state being more complex, the average oxidation states obtained from the above two assumptions still give good predictions to Ni-rich NMC with different TM ratios of both experiment measurements (Fig. 5) and DFT calculation results (Fig. 5a and 5c).

Some discrepancies will be anticipated. For example, we did not consider oxygen-redox, which may be more important in Li-excess NMC cathode. [29] Our model predicts increasing Ni^{2+} with increasing Ni-content in high-Ni NMC, which also agrees with experimental observations that Ni/Li exchange happens even more frequently with increasing Ni^{2+}. [4] While most experiments were performed in polycrystalline samples, recent synthesis with single crystalline high-Ni NMC may provide more opportunities for direct modeling and experiment comparison. [73] Based on the success of the general relationship of tracking the average valence changing of transition metals in experimental cases of NMC622 and NMC811, these equations are allowed to be applied to any other high-Ni NMC structure.

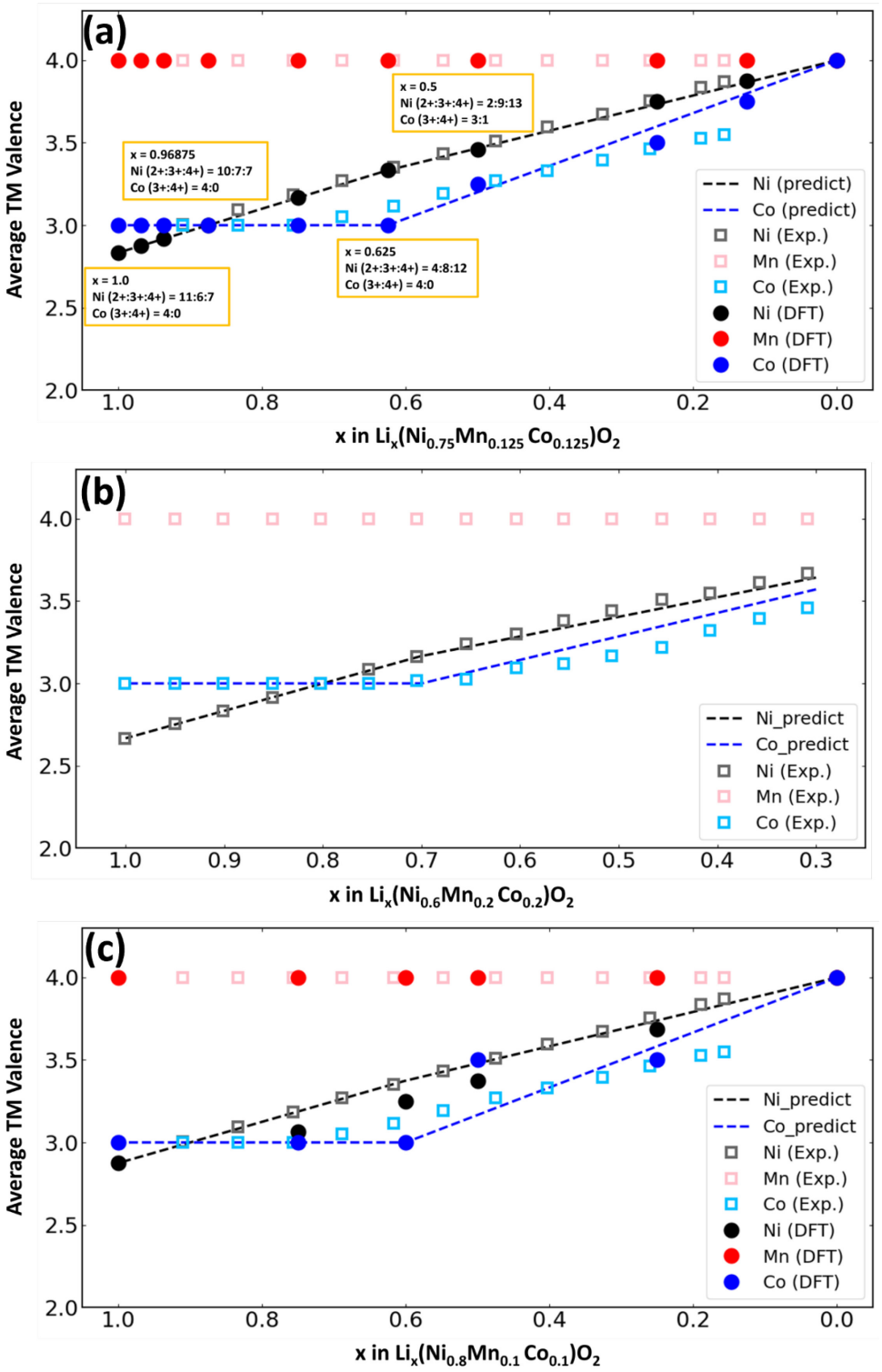

Fig 5. Transition metals (TM) average valence of (a) representative NMC811 ($LiNi_{0.75}Mn_{0.125}Co_{0.125}O_2$) built manually and experiment (West et. al.)[72], (b) NMC622 from the experiment (Tallman et. al.) [17], and (c) NMC811 ($LiNi_{0.8}Mn_{0.1}Co_{0.1}O_2$) built by MCSQS code and experiment (West et. al.) [72]. Black, red, and blue indicate Ni, Mn, and Co, respectively. Spheres and squares represent DFT results and experiment measurements, respectively, while dash lines represent the value predicted by equations listed in **Table 5.**

Table 5. TM oxidation state evolution in $Li_xNi_yMn_zCo_{1-y-z}O_2$. (with $y > 0.5$ and $y > 2z$).

x		Ni	Co
$x_c \sim 1$	Individual charges	$N_{Ni}^{n+}: \begin{cases} n=2: & x+\frac{y}{2}-1 \\ n=3: & -x+z+1 \\ n=4: & \frac{y}{2}-z \end{cases}$	$N_{Co}^{n+}: \begin{cases} n=3: & 1-y-z \\ n=4: & 0 \end{cases}$
	Average charge	$Q_{Ni}^{Avg} = 3 + \frac{1-x-z}{y}$	$Q_{Co}^{Avg} = 3$
$x_c = 1 - \frac{y}{2}$			
$0 \sim x_c$	Individual charges	$N_{Ni}^{n+}: \begin{cases} n=2: & 0 \\ n=3: & \frac{2z+y}{2-y} \cdot x \\ n=4: & y - \frac{2z+y}{2-y} \cdot x \end{cases}$	$N_{Co}^{n+}: \begin{cases} n=3: & (1-y-z) \cdot \frac{2x}{2-y} \\ n=4: & (1-y-z) \cdot (1 - \frac{2x}{2-y}) \end{cases}$
	Average charge	$Q_{Ni}^{Avg} = 4 - \frac{2z+y}{y(2-y)}x$	$Q_{Co}^{Avg} = 4 - \frac{2x}{2-y}$

4. Conclusions

It is challenging to understand the electronic structures changing in Ni-rich NMC oxides due to the fact that DFT could only barely capture the correct d-orbital ranking in a multi-component system as well as the questionable parent structure of Ni-rich NMC. In this paper, we provide a systematic way to construct the represented structure and thus allow an in-depth investigation into the electronic structures of this promising cathode material.

To systematically investigate the electronic structures of Ni-rich NMC cathode materials, DFT calculations are applied in this work. We first identify the base structure of pure $LiNiO_2$. DFT calculations are performed based on four different space groups, namely $R\bar{3}m$, *C2/m*, $P2_1/c$, and *P2/c*. It is found that the calculated band structures of the widely applied $R\bar{3}m$ is metallic regardless of the method, contrary to the experimentally reported semiconductor behavior, while *P2/c*, which allows for disproportionation of the oxidation state of Ni, is the most energetically stable and semiconducting structure of $LiNiO_2$ and thus could serve as a parent structure of its directly related compounds.

Model structures representing Ni-rich NMC are built by partially replacing Ni with Co or Mn in the *P2/c* base. Once replaced, the oxidation state of all Mn ions becomes 4+, while Co ions still maintain 3+, and part of the Ni ions become 3+ to compensate for the charge. The electronic structures of representative NMC811 confirm that, during delithiation, Ni^{2+} will lose electrons first, followed by Ni^{3+}, and Co^{3+} is the last ion that starts losing electrons. Mn^{4+} remains electrochemically inactive throughout the whole process. With these two simple assumptions, we derived a general relationship that could theoretically predict the average oxidation states of each

transition metal as a function of Lithium content. This prediction has been validated by at least two NMC compositions, suggesting it can be expanded for other high Ni-NMC compositions.

References

[1] J.B. Goodenough, K.-S. Park, *Journal of the American Chemical Society* **135** (2013) (4) 1167.

[2] O. Sekizawa, N. Kitamura, Y. Idemoto, *Electrochemistry* **78** (2010) (5) 367.

[3] S.-M. Bak, E. Hu, Y. Zhou, X. Yu, S.D. Senanayake, S.-J. Cho, K.-B. Kim, K.Y. Chung, X.-Q. Yang, K.-W. Nam, *ACS Applied Materials & Interfaces* **6** (2014) (24) 22594.

[4] J. Zheng, G. Teng, C. Xin, Z. Zhuo, J. Liu, Q. Li, Z. Hu, M. Xu, S. Yan, W. Yang, F. Pan, *The Journal of Physical Chemistry Letters* **8** (2017) (22) 5537.

[5] W. Choi, A. Manthiram, *Journal of The Electrochemical Society* **153** (2006) (9) A1760.

[6] M.D. Radin, S. Hy, M. Sina, C. Fang, H. Liu, J. Vinckeviciute, M. Zhang, M.S. Whittingham, Y.S. Meng, A. Van der Ven, *Advanced Energy Materials* **7** (2017) (20) 1602888.

[7] K. Kang, Y.S. Meng, J. Bréger, C.P. Grey, G. Ceder, *Science* **311** (2006) (5763) 977.

[8] K. Kang, G. Ceder, *Physical Review B* **74** (2006) (9) 094105.

[9] M.K. Aydinol, A.F. Kohan, G. Ceder, *Journal of Power Sources* **68** (1997) (2) 664.

[10] J.-M. Kim, H.-T. Chung, *Electrochimica Acta* **49** (2004) (6) 937.

[11] H. Kobayashi, Y. Arachi, S. Emura, H. Kageyama, K. Tatsumi, T. Kamiyama, *Journal of Power Sources* **146** (2005) (1) 640.

[12] W.-S. Yoon, M. Balasubramanian, K.Y. Chung, X.-Q. Yang, J. McBreen, C.P. Grey, D.A. Fischer, *Journal of the American Chemical Society* **127** (2005) (49) 17479.

[13] N. Yabuuchi, Y. Makimura, T. Ohzuku, *Journal of The Electrochemical Society* **154** (2007) (4) A314.

[14] Y. Koyama, I. Tanaka, H. Adachi, Y. Makimura, T. Ohzuku, *Journal of Power Sources* **119-121** (2003) 644.

[15] A. Deb, U. Bergmann, S.P. Cramer, E.J. Cairns, *Journal of The Electrochemical Society* **154** (2007) (6) A534.

[16] C.D. Quilty, G.P. Wheeler, L. Wang, A.H. McCarthy, S. Yan, K.R. Tallman, M.R. Dunkin, X. Tong, S. Ehrlich, L. Ma, K.J. Takeuchi, E.S. Takeuchi, D.C. Bock, A.C. Marschilok, *ACS Applied Materials & Interfaces* **13** (2021) (43) 50920.

[17] K.R. Tallman, G.P. Wheeler, C.J. Kern, E. Stavitski, X. Tong, K.J. Takeuchi, A.C. Marschilok, D.C. Bock, E.S. Takeuchi, *The Journal of Physical Chemistry C* **125** (2021) (1) 58.

[18] C.D. Quilty, P.J. West, G.P. Wheeler, L.M. Housel, C.J. Kern, K.R. Tallman, L. Ma, S. Ehrlich, C. Jaye, D.A. Fischer, K.J. Takeuchi, D.C. Bock, A.C. Marschilok, E.S. Takeuchi, *Journal of The Electrochemical Society* **169** (2022) (2) 020545.

[19] R.D. Leapman, L.A. Grunes, P.L. Fejes, *Physical Review B* **26** (1982) (2) 614.

[20] H. Tan, J. Verbeeck, A. Abakumov, G. Van Tendeloo, *Ultramicroscopy* **116** (2012) 24.

[21] J. Abed, S. Ahmadi, L. Laverdure, A. Abdellah, C.P. O'Brien, K. Cole, P. Sobrinho, D. Sinton, D. Higgins, N.J. Mosey, S.J. Thorpe, E.H. Sargent, *Advanced Materials* **33** (2021) (45) 2103812.

[22] S. Carenco, C.S. Bonifacio, J.C. Yang, *Chemistry – A European Journal* **24** (2018) (46) 12037.

[23] B. Rellinghaus, S. Stappert, E.F. Wassermann, H. Sauer, B. Spliethoff, *The European Physical Journal D - Atomic, Molecular, Optical and Plasma Physics* **16** (2001) (1) 249.

[24] L.A.J. Garvie, A.J. Craven, *Physics and Chemistry of Minerals* **21** (1994) (4) 191.

[25] J.H. Rask, B.A. Miner, P.R. Buseck, *Ultramicroscopy* **21** (1987) (4) 321.

[26] M.M. Grush, Y. Muramatsu, J.H. Underwood, E.M. Gullikson, D.L. Ederer, R.C.C. Perera, T.A. Callcott, *Journal of Electron Spectroscopy and Related Phenomena* **92** (1998) (1) 225.

[27] B. Gilbert, B.H. Frazer, A. Belz, P.G. Conrad, K.H. Nealson, D. Haskel, J.C. Lang, G. Srajer, G. De Stasio, *The Journal of Physical Chemistry A* **107** (2003) (16) 2839.

[28] J. Lee, B. Kim, B.H. Kim, B.I. Min, S. Kolesnik, O. Chmaissem, J. Mais, B. Dabrowski, H.J. Shin, D.H. Kim, H.J. Lee, J.S. Kang, *Physical Review B* **80** (2009) (20) 205112.

[29] D.-H. Seo, J. Lee, A. Urban, R. Malik, S. Kang, G. Ceder, *Nature Chemistry* **8** (2016) (7) 692.

[30] I.M. Markus, F. Lin, K.C. Kam, M. Asta, M.M. Doeff, *The Journal of Physical Chemistry Letters* **5** (2014) (21) 3649.
[31] F. Kong, R.C. Longo, M.-S. Park, J. Yoon, D.-H. Yeon, J.-H. Park, W.-H. Wang, S. Kc, S.-G. Doo, K. Cho, *Journal of Materials Chemistry A* **3** (2015) (16) 8489.
[32] M. Dixit, M. Kosa, O.S. Lavi, B. Markovsky, D. Aurbach, D.T. Major, *Physical Chemistry Chemical Physics* **18** (2016) (9) 6799.
[33] H. Sun, K. Zhao, *The Journal of Physical Chemistry C* **121** (2017) (11) 6002.
[34] T. Kim, *Journal of Solid State Chemistry* **310** (2022) 123040.
[35] A. Rougier, C. Delmas, A.V. Chadwick, *Solid State Communications* **94** (1995) (2) 123.
[36] J.H. Chung, T. Proffen, S. Shamoto, A.M. Ghorayeb, L. Croguennec, W. Tian, B.C. Sales, R. Jin, D. Mandrus, T. Egami, *Physical Review B* **71** (2005) (6) 064410.
[37] S. Laubach, S. Laubach, P.C. Schmidt, D. Ensling, S. Schmid, W. Jaegermann, A. Thißen, K. Nikolowski, H. Ehrenberg, *Physical Chemistry Chemical Physics* **11** (2009) (17) 3278.
[38] A.R. Genreith-Schriever, A. Alexiu, G.S. Phillips, C.S. Coates, L.A.V. Nagle-Cocco, J.D. Bocarsly, F.N. Sayed, S.E. Dutton, C.P. Grey, *Chemistry of Materials* **36** (2024) (5) 2289.
[39] H. Chen, C.L. Freeman, J.H. Harding, *Physical Review B* **84** (2011) (8) 085108.
[40] L. de Biasi, A. Schiele, M. Roca-Ayats, G. Garcia, T. Brezesinski, P. Hartmann, J. Janek, *ChemSusChem* **12** (2019) (10) 2240.
[41] K. Mukai, Y. Kishida, H. Nozaki, K. Dohmae, *Chemistry of Materials* **25** (2013) (14) 2828.
[42] S. Sicolo, M. Mock, M. Bianchini, K. Albe, *Chemistry of Materials* **32** (2020) (23) 10096.
[43] A.L. Barra, G. Chouteau, A. Stepanov, A. Rougier, C. Delmas, *The European Physical Journal B - Condensed Matter and Complex Systems* **7** (1999) (4) 551.
[44] M. Bonda, M. Holzapfel, S. de Brion, C. Darie, T. Fehér, P.J. Baker, T. Lancaster, S.J. Blundell, F.L. Pratt, *Physical Review B* **78** (2008) (10) 104409.
[45] K. Foyevtsova, I. Elfimov, J. Rottler, G.A. Sawatzky, *Physical Review B* **100** (2019) (16) 165104.
[46] G. Kresse, J. Furthmüller, *Computational Materials Science* **6** (1996) (1) 15.
[47] G. Kresse, J. Furthmüller, *Physical Review B* **54** (1996) (16) 11169.
[48] M. Dixit, B. Markovsky, D. Aurbach, D.T. Major, *Journal of The Electrochemical Society* **164** (2017) (1) A6359.
[49] J.-M. Lim, T. Hwang, D. Kim, M.-S. Park, K. Cho, M. Cho, *Scientific Reports* **7** (2017) (1) 39669.
[50] B. Han, B. Key, S.H. Lapidus, J.C. Garcia, H. Iddir, J.T. Vaughey, F. Dogan, *ACS Applied Materials & Interfaces* **9** (2017) (47) 41291.
[51] F. Schipper, M. Dixit, D. Kovacheva, M. Talianker, O. Haik, J. Grinblat, E.M. Erickson, C. Ghanty, D.T. Major, B. Markovsky, D. Aurbach, *Journal of Materials Chemistry A* **4** (2016) (41) 16073.
[52] F. Schipper, H. Bouzaglo, M. Dixit, E.M. Erickson, T. Weigel, M. Talianker, J. Grinblat, L. Burstein, M. Schmidt, J. Lampert, C. Erk, B. Markovsky, D.T. Major, D. Aurbach, *Advanced Energy Materials* **8** (2018) (4) 1701682.
[53] A. Tornheim, S. Sharifi-Asl, J.C. Garcia, J. Bareño, H. Iddir, R. Shahbazian-Yassar, Z. Zhang, *Nano Energy* **55** (2019) 216.
[54] L. Wang, T. Maxisch, G. Ceder, *Physical Review B* **73** (2006) (19) 195107.
[55] A. Jain, G. Hautier, S.P. Ong, C.J. Moore, C.C. Fischer, K.A. Persson, G. Ceder, *Physical Review B* **84** (2011) (4) 045115.
[56] M.W. Swift, Y. Qi, *Physical Review Letters* **122** (2019) (16) 167701.
[57] M. Aykol, S. Kim, C. Wolverton, *The Journal of Physical Chemistry C* **119** (2015) (33) 19053.
[58] K. Min, S.-W. Seo, Y.Y. Song, H.S. Lee, E. Cho, *Physical Chemistry Chemical Physics* **19** (2017) (3) 1762.
[59] S. Ziraki, M. Moaddeli, M. Kanani, B. Hashemi, *Physica Scripta* **97** (2022) (12) 125819.
[60] T. Das, J.D. Nicholas, Y. Qi, *Journal of Materials Chemistry A* **5** (2017) (9) 4493.
[61] J. Molenda, P. Wilk, J. Marzec, *Solid State Ionics* **146** (2002) (1) 73.
[62] J.B. Goodenough, Y. Kim, *Chemistry of Materials* **22** (2010) (3) 587.
[63] B.J. Hwang, Y.W. Tsai, D. Carlier, G. Ceder, *Chemistry of Materials* **15** (2003) (19) 3676.
[64] A. van de Walle, P. Tiwary, M. de Jong, D.L. Olmsted, M. Asta, A. Dick, D. Shin, Y. Wang, L.Q. Chen, Z.K. Liu, *Calphad* **42** (2013) 13.
[65] I.A. Courtney, J.S. Tse, O. Mao, J. Hafner, J.R. Dahn, *Physical Review B* **58** (1998) (23) 15583.
[66] L. Croguennec, C. Pouillerie, C. Delmas, *Journal of The Electrochemical Society* **147** (2000) (4) 1314.
[67] K. Märker, P.J. Reeves, C. Xu, K.J. Griffith, C.P. Grey, *Chemistry of Materials* **31** (2019) (7) 2545.

[68] S. Buechele, E. Logan, T. Boulanger, S. Azam, A. Eldesoky, W. Song, M.B. Johnson, M. Metzger, *Journal of The Electrochemical Society* **170** (2023) (1) 010518.
[69] R. Hausbrand, G. Cherkashinin, H. Ehrenberg, M. Gröting, K. Albe, C. Hess, W. Jaegermann, *Materials Science and Engineering: B* **192** (2015) 3.
[70] K.M. Nikolowski, N. Bramnik, C. Baehtz, H. Ehrenberg, H. Fuess, *ECS Transactions* **1** (2006) (26) 17.
[71] Y. Mo, L. Guo, B. Cao, Y. Wang, L. Zhang, X. Jia, Y. Chen, *Energy Storage Materials* **18** (2019) 260.
[72] P.J. West, C.D. Quilty, Z. Wang, S.N. Ehrlich, L. Ma, C. Jaye, D.A. Fischer, X. Tong, A.M. Kiss, E.S. Takeuchi, A.C. Marschilok, K.J. Takeuchi, D.C. Bock, *The Journal of Physical Chemistry C* **127** (2023) (15) 7054.
[73] Y. Bi, J. Tao, Y. Wu, L. Li, Y. Xu, E. Hu, B. Wu, J. Hu, C. Wang, J.-G. Zhang, Y. Qi, J. Xiao, *Science* **370** (2020) (6522) 1313.

Acknowledgment
We thank the Center for Computation and Visualization (CCV) at Brown University and the High-Performance Computing at the National Renewable Energy Lab for computational facilities. The initial work and Y.W were supported by NSF-DMR-2054441. I.H, B.L and Y.Q thank the financial support from the Assistant Secretary for Energy Efficiency and Renewable Energy, Office of Vehicle Technologies of the U.S. Department of Energy (DOE) through the Cathode-Electrolyte Interphase (CEI) Consortium. B.L also thanks the financial support from the Laboratory Directed Research and Development Program of ORNL, managed by UT-Battelle, LLC, for the U. S. Department of Energy. A portion of this manuscript has been authored by Oak Ridge National Laboratory (ORNL), managed by UT-Battelle, under contract DE-AC05-00OR22725 with the US Department of Energy (DOE). The US government retains and the publisher, by accepting the article for publication, acknowledges that the US government retains a nonexclusive, paid-up, irrevocable, worldwide license to publish or reproduce the published form of this manuscript or allow others to do so, for US government purposes. DOE will provide public access to these results of federally sponsored research in accordance with the DOE Public Access Plan (https://www.energy.gov/doe-public-access-plan).